Available online at www.sciencedirect.com
ScienceDirect
Trans. Nonferrous Met. Soc. China 35(2025) 4166−4183

Transactions of Nonferrous Metals Society of China
www.tnmsc.cn

# Simultaneously enhancing mechanical properties and electrical conductivity of $TiB_2$/Cu composites via submicron laminated structure

Fei HAN[1,2,3], Yi-hui JIANG[1,2,3], Fei CAO[1,2,3], Hao SHI[1,2,3], Lei CAI[1,2,3], Shu-hua LIANG[1,2,3]

1. School of Materials Science and Engineering, Xi'an University of Technology, Xi'an 710048, China;
2. Engineering Research Center of Conducting Materials and Composite Technology, Ministry of Education,
Xi'an University of Technology, Xi'an 710048, China;
3. Shaanxi Provincial Key Laboratory of Electrical Materials and Infiltration Technology,
Xi'an University of Technology, Xi'an 710048, China

Received 29 March 2024; accepted 13 November 2024

---

**Abstract:** Copper matrix composites prepared via traditional methods face mechanical property and electrical conductivity trade-off problems. In this study, $TiB_2$/Cu−Cu heterogeneous laminated composites with submicron lamellar thicknesses were prepared via flake powder metallurgy (FPM) using gas-atomized in situ composite powders as raw material. By thermal mismatch strengthening, and the geometrically necessary dislocations (GNDs) generated by mechanically incompatible deformation between adjacent heterogeneous lamellae and their interaction with statistically stored dislocations (SSDs), the as-prepared $TiB_2$/Cu−Cu submicron laminated composites (SLCs) exhibit significantly enhanced mechanical properties. At the same time, the interaction and propagation of multimode cracks provide extrinsic toughening for SLCs. The pure Cu lamellae with low density grain boundaries and dislocations and no $TiB_2$ particles provide a channel with little electron scattering for the rapid transport of carriers, thereby ensuring high electrical conductivity.

**Key words:** submicron laminated composites; thermal mismatch strengthening; incompatible deformation; hetero-deformation induced strengthening; crack propagation

---

## 1 Introduction

$TiB_2$ ceramic particles have a high elastic modulus (574 GPa) and high hardness (30 GPa) [1,2], and consequently have been widely used as reinforcements for the preparation of high-strength Ti [3], Fe [4], Mg [5], Al [6] and Cu [7] matrix composites. However, for the $TiB_2$ particle-reinforced Cu matrix composites used for power transmission applications, on the one hand, the elastic-plastic deformation between the micron-scale $TiB_2$ particles and the Cu matrix led to local stress concentration and strain localization, which greatly reduced the ductility and damage tolerance of the Cu matrix composites [8]. On the other hand, although the Cu matrix can be strengthened by introducing a variety of defects, heterogeneous particles and composite interfaces, the electrical conductivity is greatly reduced because of the sharp increase in the number of electron scattering centers [9]. Therefore, $TiB_2$ particle-reinforced Cu matrix composites face trade-offs among strength, ductility and electrical conductivity [10,11].

To improve the synergistic relationship among strength, ductility and electrical conductivity, copper matrix composites are achieved through size refinement, dispersion distribution and composite

---

**Corresponding author:** Shu-hua LIANG, Tel: +86-13891430199, E-mail: liangsh@xaut.edu.cn;
Yi-hui JIANG, Tel: +86-13891941017, E-mail: jiangyihui@xaut.edu.cn

https://doi.org/10.1016/S1003-6326(25)66936-6

interface regulation of the reinforcement [12−15]. At present, in situ preparation technology has been proven to be an effective means of preparing reinforcements with better wettability at the composite interface [7,12]. The research by CAO et al [13] revealed that in situ $TiB_2$ particles generated by casting can prevent interface pollution between the particles and the matrix. JIANG et al [14] reported that in situ powder metallurgy can achieve the size refinement and dispersion distribution of $TiB_2$ particles. However, the low cooling rate of conventional casting leads to large $TiB_2$ particles, and the segregation and agglomeration of particles easily occur during the solidification [15]. The conventional powder metallurgy always involves introducing impurities and reducing the ductility and electrical conductivity of composites [16].

In recent years, researchers have gradually realized the important role of biomimetic laminated construction in achieving synergy among the strength, ductility and electrical conductivity of copper matrix composites [17−19]. CAO et al [17] prepared Gr/Cu nanoscale laminated composites by in situ growth of high-quality graphene on the surface of copper sheets, which significantly improved the strength without sacrificing ductility and electrical conductivity. HAN et al [18] achieved CuCrZr/Cu laminated composites with a high matching index of strength, ductility and electrical conductivity by designing an alternating laminated arrangement between hard CuCrZr components and soft pure Cu components. Thus far, laminated structures can achieve strengthening and toughening while ensuring excellent conductivity. The design of submicron or even nanometer heterogeneous interface spacings has been proposed based on the existence of heterogeneous interface-affected zones, which can help to achieve significant strengthening and toughening [20−22]. However, the low solidification rate during traditional casting, the Cu−Ti micromolten pool and the diffusion of B during traditional powder metallurgy make the distribution of in situ $TiB_2$ particles in the Cu matrix uncontrollable [8,15,23]. Therefore, the preparation of $TiB_2$/Cu laminated composites with a small heterogeneous interface spacing via traditional in situ technology faces great challenges.

Recently, an in situ metal matrix composite powder prepared by rapid gas atomization solidification has been developed [24,25], which provides the possibility for the preparation of laminated metal matrix composites with a small heterogeneous interface spacing. In this study, an in situ $TiB_2$/Cu composite powder was used as the raw materials, and a $TiB_2$/Cu−Cu laminated composite with a submicron heterogeneous interface spacing was firstly prepared via flake powder metallurgy (FPM). The mechanical properties, electrical conductivity and incompatible tensile deformation of the $TiB_2$/Cu−Cu submicron laminated composites (SLCs) were subsequently analyzed. Finally, the synergistic mechanism among the strength, ductility and electrical conductivity of the SLC was revealed. The FPM based on in situ composite powders provides an effective way to prepare high-performance laminated copper matrix composites with submicron heterogeneous interfaces spacings.

## 2 Experimental

Spherical in situ $TiB_2$/Cu composite powders (2 wt.% $TiB_2$, 20−75 μm) and commercial spherical pure Cu powders (99.9 wt.%, 20−75 μm) were selected as the raw materials. Figure 1 shows the preparation process of the $TiB_2$/Cu−Cu submicron laminated composites, which involves four steps: (1) The in situ $TiB_2$/Cu composite powders were prepared by rapid solidification of Cu−B and Cu−Ti master alloy mixed melts atomized by high-pressure Ar gas flow (99.9 wt.%, atomization pressure of 5 MPa) (Fig. 1(a)). (2) The initial powder was subjected to flake treatment (Fig. 1(d)). The spherical in situ $TiB_2$/Cu composite powder and the spherical pure Cu powder were mixed and milled at a mass ratio of 1:1, which can easily yield a mixed powder of flake $TiB_2$/Cu and flake pure Cu. The milling environment and process control agent were Ar gas and $C_2H_5OH$, respectively. The milling frequency and time were 50 Hz and 2.5 h, respectively. (3) The flake powder was subjected to hot-pressing consolidation (Fig. 1(e)). $TiB_2$/Cu−Cu laminated composites were prepared via hot-press sintering of mixed flake powders. Sintering was carried out at 1020 °C for 40 min, and the samples were pressed at 35 MPa in a nitrogen atmosphere. (4) Rolling deformation densification was performed (Fig. 1(f)). The rolling deformation process includes

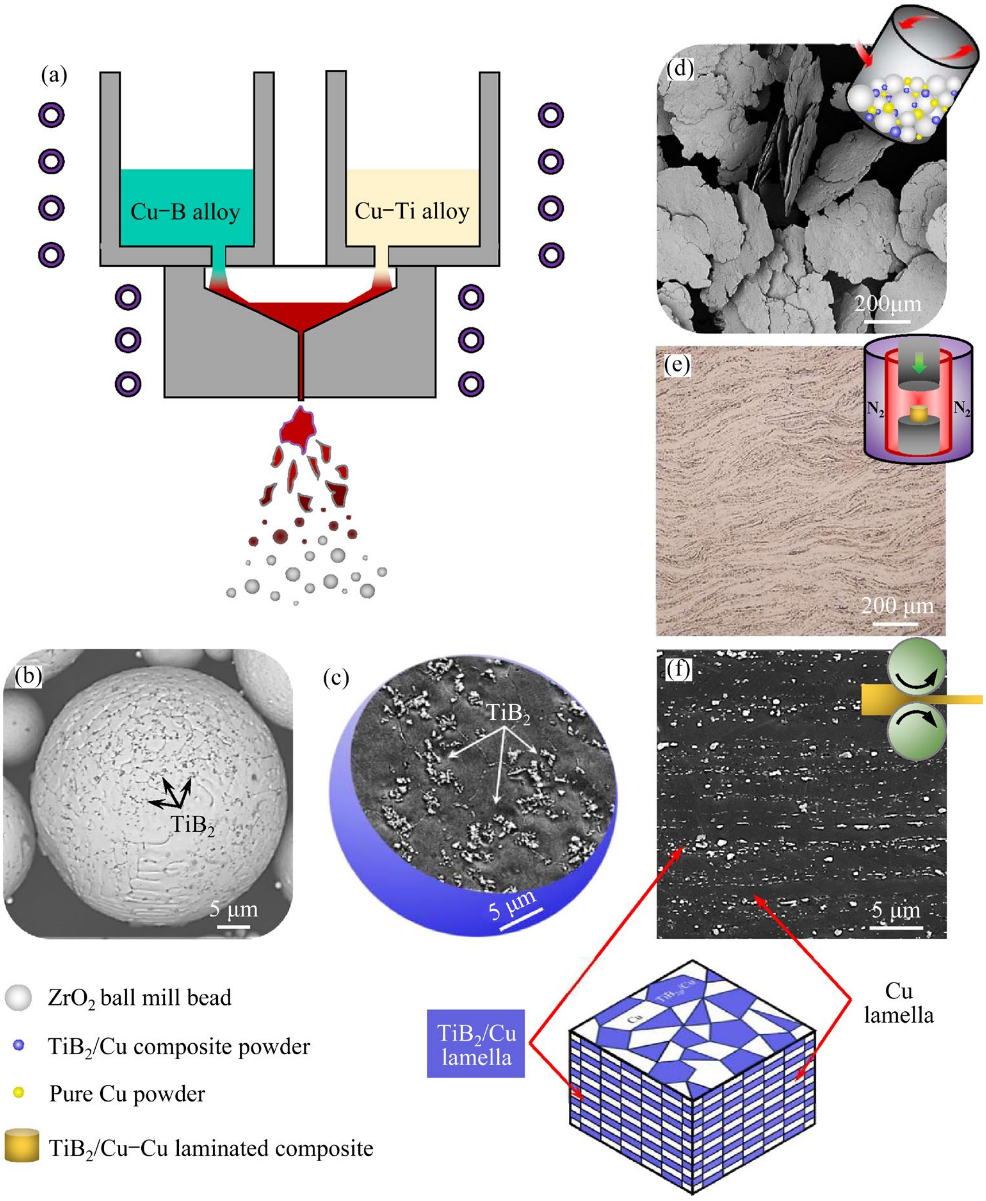

**Fig. 1** Microstructures of $TiB_2$/Cu−Cu SLCs at each preparation stage: (a) Schematic diagram of in situ $TiB_2$/Cu composite powder prepared by gas atomization; (b) Surface of $TiB_2$/Cu composite powder; (c) Cross-sectional microstructure of $TiB_2$/Cu composite powder; (d) Mixed powders of flake $TiB_2$/Cu and flake pure Cu; (e) Microstructure of sintered laminated composite; (f) Microstructure of SLC after rolling

first high temperature rolling at 900 °C with a 50% reduction and then room temperature rolling with a 30% reduction. The $TiB_2$/Cu−Cu SLCs after rolling were annealed at 300, 360 and 420 °C for 1 h, which are referred to as SLC-300 °C, SLC-360 °C and SLC-420 °C, respectively, for convenience. For comparison, homogeneous 2 wt.% $TiB_2$/Cu composites ($TiB_2$/Cu for short) and pure Cu were prepared via the same process as the SLC and referred to as $TiB_2$/Cu-300 °C, $TiB_2$/Cu-360 °C and $TiB_2$/Cu-420 °C, and Cu-300 °C, pure Cu-360 °C and Cu-420 °C, respectively.

To ensure the relative density of the composite sample after rolling deformation, the sample surface was firstly polished with sandpaper to be clean and free of impurities, and then the actual density of the sample was measured via the Archimedes drainage method with an electronic balance (accuracy: 0.0001 g, FA1104J). Finally, the ratio of the actual density to the theoretical density was calculated, that is, the relative density of the sample. The microstructures of the in situ $TiB_2$/Cu composite powder and the tensile fracture and fracture cross section of the SLC were characterized via optical microscopy (OM; GX71), scanning electron microscopy (SEM; JSM6700F) and scanning transmission electron microscopy (TEM; FEI TECNAI G2 F20). The OM and SEM samples were electrolytically etched in a chemical etching solution ($H_3PO_4 + C_2H_5OH$) for 15 s after mechanical polishing. The TEM samples were initially thinned by mechanical grinding and then thinned with a Gatan 691 ion thinner. The microstructure evolution of the SLC was characterized by electron back-scattered diffraction (EBSD) with a step length of 60 nm. The EBSD samples were vibrationally polished in a dilute solution of colloidal silica for 2 h after mechanical polishing. All SLC samples were observed on the ND−RD plane.

The SLC samples were subjected to both normal and unloading–reloading tensile tests via a tensile testing machine (AG-IC 100 kN) with a tensile rate of 0.6 mm/min at room temperature. The tensile samples were cut along the rolling direction on the TD−RD plane. The dimensions of the gauge part were 12 mm × 3 mm × 1 mm. The electrical conductivity was measured on the TD−RD plane of the sample by an eddy current instrument (Sigma 2008B) and expressed according to the International Annealed Copper Standard (IACS). The tensile and electrical conductivity tests were repeated for at least three samples to ensure data reproducibility.

## 3 Results

### 3.1 Microstructural evolution during FPM processing

The microstructures of the $TiB_2$/Cu−Cu SLCs at each preparation stage are shown in Fig. 1. The reinforcement particles in the in situ $TiB_2$/Cu composite powder prepared by gas atomization form microclusters at the grain boundaries (black arrows in Fig. 1(b) and white arrows in Fig. 1(c)), which should be the $TiB_2$ particles formed by the reaction of the Ti and B atoms during the mixing of the Cu−Ti and Cu−B master alloy melts. The average size of the reinforcement particles is approximately 270 nm. As shown in Fig. 1(d), the as-prepared flake $TiB_2$/Cu composite powders or flake pure Cu powders have a 2D planar morphology with an average diameter of approximately 395 μm and a large aspect ratio (ratio of diameter to thickness) of 172. Owing to the use of ethanol as a process control agent during ball milling, the as-prepared flake powders tend to be individual platelets, which is helpful for the alignment and consolidation of the flake powders. The optical microstructure of as-sintered laminated composites is an alternating wavy structure with $TiB_2$/Cu lamellae and pure Cu lamellae (Fig. 1(e)). After rolling deformation, the $TiB_2$/Cu−Cu composites achieved a high relative density (>99%) and laminated structure. The average thickness of the pure Cu lamellae was less than 1 μm, approximately 700 nm (Fig. 1(f)). These findings indicate that FPM can be used to construct a submicron heterogeneous laminated structure.

### 3.2 Heterogeneous microstructures of SLCs

Figure 2 shows the EBSD maps of the $TiB_2$/Cu−Cu SLCs after annealing at different temperatures. A heterogeneous microstructure of fine-grained lamellae (the areas within the white circles in Fig. 2), alternating sequentially with coarse-grained lamellae, is formed in all of the SLCs after annealing (Figs. 2($a_1$, $b_1$, $c_1$)). The inverse pole figures (IPFs) of the SLCs reveal the fully recrystallized microstructure of pure Cu lamellae (Figs. 2($a_1$, $b_1$, $c_1$)). As the annealing temperature increases from 300 to 420 °C, the grains of the pure Cu lamellae significantly coarsen, and the average grain size increases from 530 nm to 1.1 μm. The grain boundaries in pure Cu lamellae migrate mainly in the RD direction because the grain growth is hindered by reinforcements in adjacent $TiB_2$/Cu lamellae. The grain size of the $TiB_2$/Cu lamellae does not change significantly, and the lamellae are still nanograins. This is mainly because $TiB_2$ particles increase the stacking fault energy of the Cu grains [26], thereby improving their thermal stability. In addition, after annealing, the $TiB_2$/Cu lamellae always maintain a random orientation. However, the $\langle 101 \rangle$ orientation of the pure Cu lamellae is enhanced as the annealing temperature increases (Fig. 2($c_1$)). A comparison of the pole figures reveals that the (100) basal planes of SLC-300 °C and SLC-360 °C have the strongest texture intensities (Figs. 2($a_2$, $b_2$)), whereas the (111) basal plane of SLC-420 °C has the strongest texture intensity (Fig. 2($c_2$)). The texture intensity of the basal plane gradually increases with increasing annealing temperature, which is mainly because the growth of grains in pure Cu lamellae is constrained

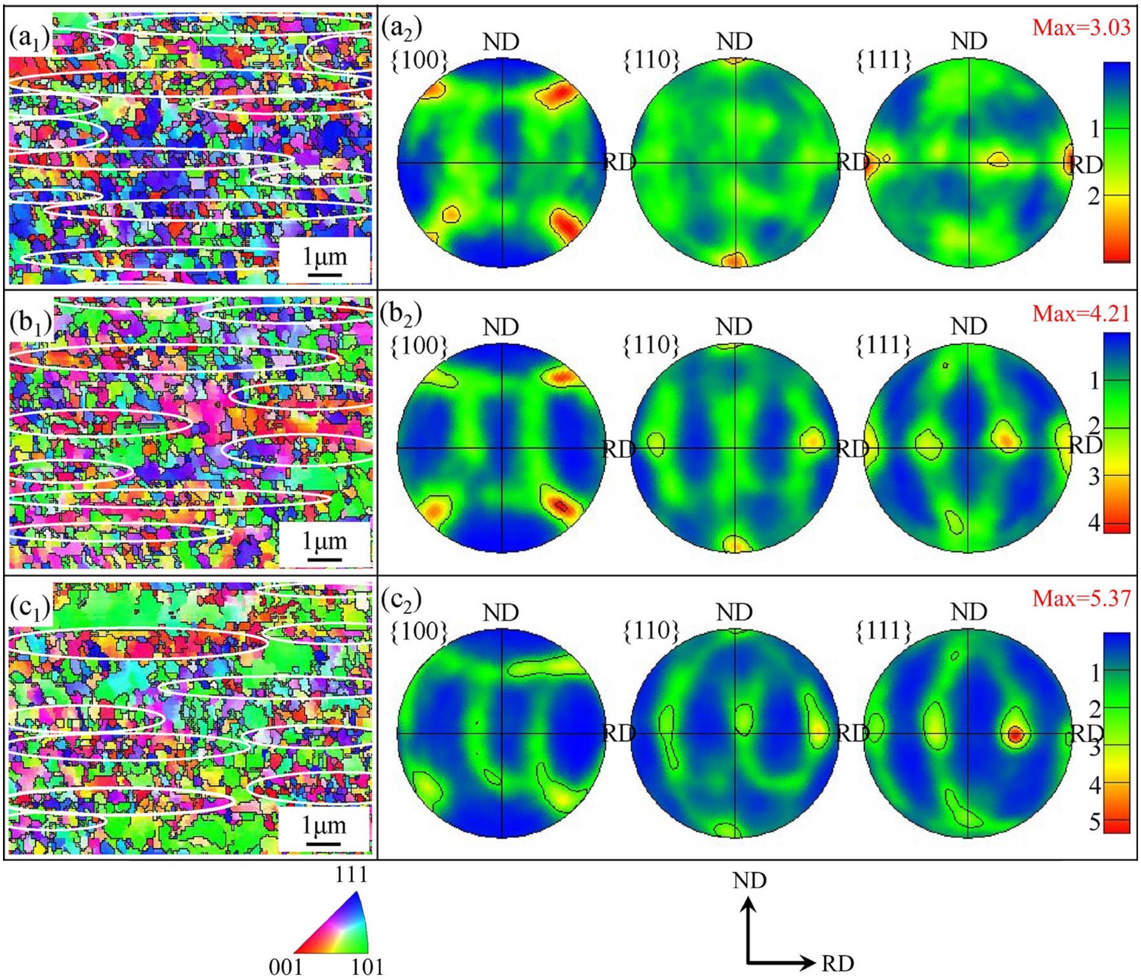

**Fig. 2** EBSD maps of $TiB_2$/Cu−Cu SLCs after annealing at different temperatures: ($a_1$, $b_1$, $c_1$) Inverse pole figures and grain morphologies of SLC-300 °C, SLC-360 °C and SLC-420 °C, respectively; ($a_2$, $b_2$, $c_2$) Pole figures corresponding to ($a_1$, $b_1$, $c_1$), respectively

by the adjacent $TiB_2$/Cu lamellae in the direction perpendicular to the RD direction [27]. The difference in grain size and crystal orientation between the $TiB_2$/Cu lamellae and pure Cu lamellae indicates the difference in mechanical properties between the adjacent heterogeneous lamellae, which can contribute to a significant hetero-deformation induced (HDI) strengthening effect during plastic deformation [28].

Figure 3 shows the Schmid factor distribution of the $\{111\}\langle 1\bar{1}0\rangle$ main slip system in the $TiB_2$/Cu−Cu SLCs after annealing. The grains with a low Schmid factor in SLC-300 °C are dispersed in the $TiB_2$/Cu lamellae and pure Cu lamellae (Fig. 3(a)). In SLC-360 °C and SLC-420 °C, only the smaller equiaxed grains in the pure Cu lamellae have a relatively low Schmid factor, whereas the grains with a low Schmid factor in the $TiB_2$/Cu lamellae still exhibit a more discrete distribution (Figs. 3(b, c)). Moreover, as the annealing temperature increases, the proportion of grains with a lower Schmid factor (<0.35) in the SLC gradually decreases (Figs. 3(d−f)), which is beneficial to increasing the stability and duration of plastic deformation. Notably, the proportion of grains with a higher average Schmid factor is slightly lower in SLC-360 °C (Fig. 3(e)), which may be attributed to the local crystal misorientation caused by thermal mismatch in pure Cu lamellae, limiting the number of slip systems [29].

Figure 4 shows the TEM images of SLC-360 °C. The fine-grained lamellae are separated by coarse-grained lamellae of pure Cu with an average thickness of approximately 570 nm (Fig. 4(a)). Compared with the pure Cu lamella, there are $TiB_2$ particles with an average size

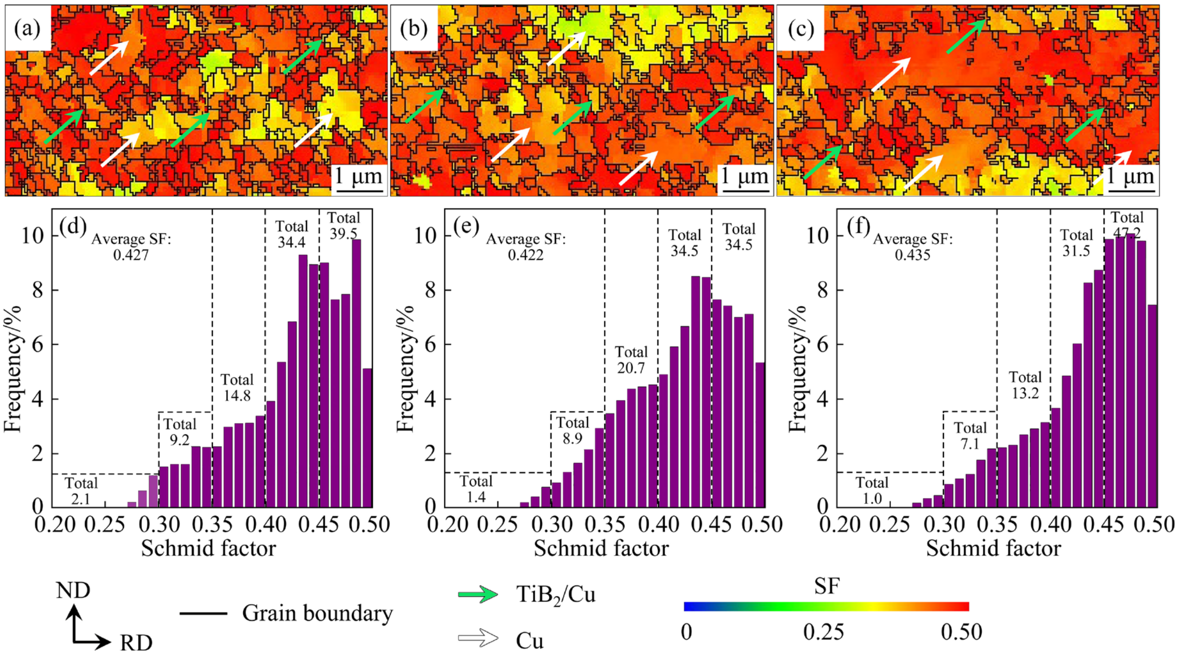

**Fig. 3** Schmid factor (SF) distribution of {111}⟨1$\bar{1}$0⟩ main slip system in $TiB_2$/Cu−Cu SLCs: (a, b, c) Schmid factor distributions of SLC-300 °C, SLC-360 °C and SLC-420 °C, respectively; (d, e, f) Statistical results of Schmid factors corresponding to (a, b, c), respectively

of approximately 270 nm in the fine-grained lamella (Fig. 4(b)), which are dispersed at the grain boundaries and within the grains (Figs. 4(d−f)). The particles in the $TiB_2$/Cu composite powders, as the only source of reinforcement, are $TiB_2$ (Figs. 1(b, c)). However, compared with that of the $TiB_2$ particles in the composite powders, the distribution of $TiB_2$ particles in the SLC is more uniform. This is attributed mainly to the flattening or stretching of the $TiB_2$/Cu composite powders during ball milling and rolling deformation, which promotes the separation of the $TiB_2$ particle clusters at the grain boundaries. Moreover, the $TiB_2$/Cu lamellae are still elongated deformation grains, and there are many dislocations and substructures around the $TiB_2$ particles (Fig. 4(c)). In addition, there are no obvious defects in the high-resolution TEM image of the $TiB_2$−Cu interface (Fig. 4(g)), which indicates strong bonding at the interface between $TiB_2$ and Cu. The interplanar spacing of 0.204 nm on the (101) plane of the reinforcement particles again confirms that the particles are $TiB_2$ (Fig. 4(h)). Obvious dislocations are observed in the inverse fast Fourier transform (IFFT) pattern of the Cu matrix near the $TiB_2$−Cu interface (Fig. 4(i)). This is mainly because, on the one hand, rolling deformation can significantly increase the dislocation density in the composite, even if annealing recovery causes the absorption of a large number of dislocations, on the other hand, there is thermal mismatch between the Cu matrix and the $TiB_2$ particles because of the difference in the coefficients of thermal expansion (CTE), resulting in the generation of geometrically necessary dislocations (GNDs) near the $TiB_2$−Cu interface during cooling after annealing [30,31]. Notably, $TiB_2$ particles hinder the movement of dislocations, and the dislocations generated by thermal mismatch improve the yield strength of the SLC.

### 3.3 Mechanical properties and electrical conductivity of SLCs

Figure 5 shows the tensile properties and electrical conductivity of the $TiB_2$/Cu−Cu SLCs, homogeneous $TiB_2$/Cu composites and pure Cu materials after annealing. Table 1 lists the mechanical properties of the samples prepared in this study. With increasing annealing temperature, the ultimate tensile strength (UTS) of $TiB_2$/Cu and pure Cu decreased gradually, whereas the fracture elongation (FE) increased gradually (Fig. 5(a) and Table 1). This is attributed mainly to the reduction in the number of deformed dislocations and the growth of grains caused by annealing. However,

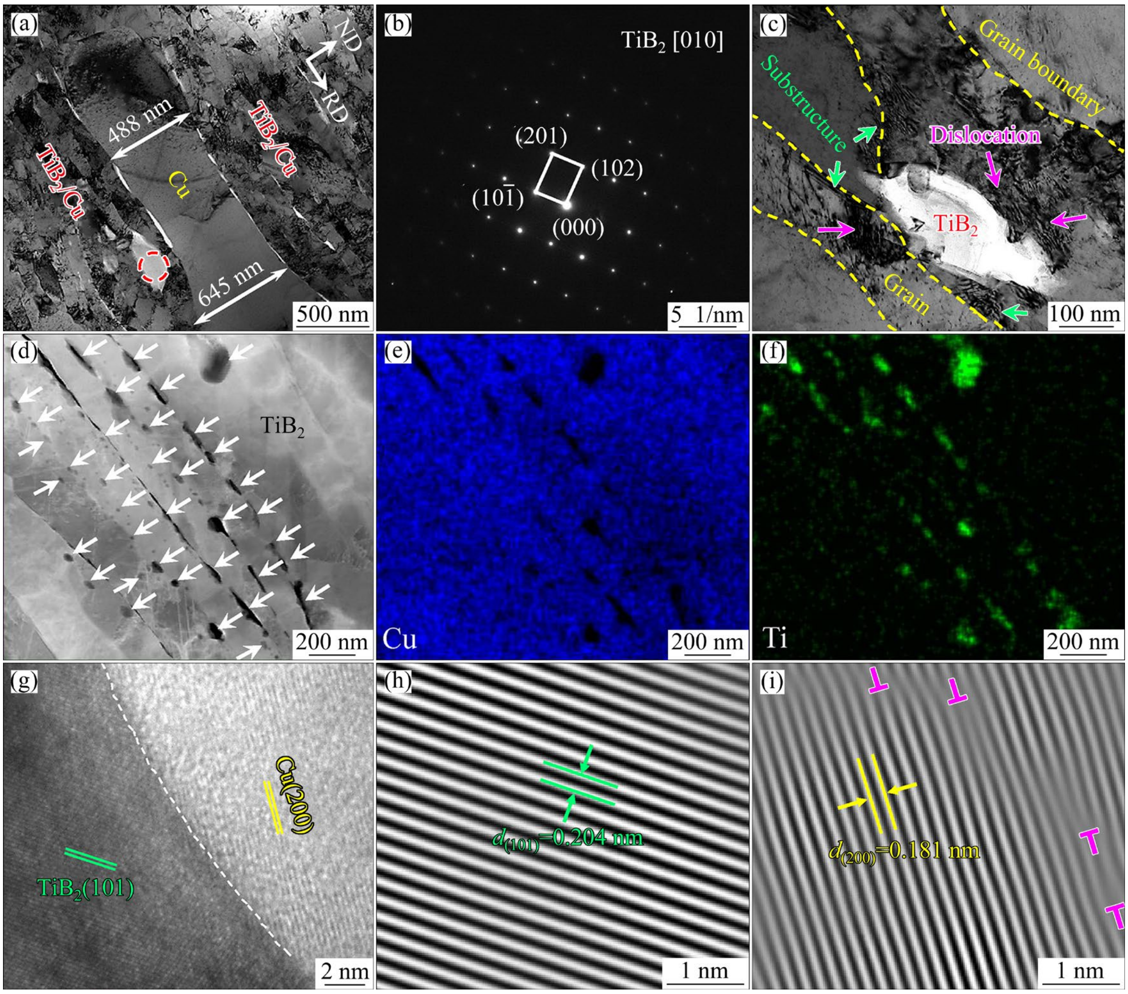

**Fig. 4** TEM images of SLC-360 °C: (a) Bright-field TEM image of submicron laminated microstructure; (b) Selected area electron diffraction (SAED) pattern of particles in red region of (a); (c) Dislocations and substructures near $TiB_2$ particles; (d) Distribution of $TiB_2$ particles at grain boundaries and within grains; (e, f) Distribution of Cu and Ti elements in (d), respectively; (g) High-resolution TEM image of interface between Cu and $TiB_2$; (h) IFFT pattern of $TiB_2$ particles showing lattice spacing; (i) IFFT pattern of Cu matrix near Cu−$TiB_2$ interface showing lattice spacing and number of dislocations

when the annealing temperature increases from 300 to 420 °C, the SLCs exhibit extraordinary strength and ductility. Compared with homogeneous $TiB_2$/Cu composites, SLC-360 °C can improve the UTS without sacrificing the FE, and SLC-420 °C can improve the FE without sacrificing the UTS (Figs. 5(a, b) and Table 1). These findings indicate that the submicron laminated structure overcomes the trade-off between strength and ductility. Moreover, the yield strength (YS, $\sigma_{0.2}$) of the SLC was predicted via Eq. (1) based on the rule of mixtures (ROM):

$$\sigma_{0.2,\mathrm{ROM}}=\sigma_{0.2,\mathrm{TiB_2/Cu}}V_{\mathrm{TiB_2/Cu}}+\sigma_{0.2,\mathrm{Cu}}V_{\mathrm{Cu}} \quad (1)$$

where $\sigma_{0.2,\mathrm{ROM}}$ is the predicted YS of the SLC; $\sigma_{0.2,\mathrm{TiB_2/Cu}}$ and $\sigma_{0.2,\mathrm{Cu}}$ are the YS of the homogeneous $TiB_2$/Cu composite and pure Cu components, respectively; $V_{\mathrm{TiB_2/Cu}}$ and $V_{\mathrm{Cu}}$ are the volume fractions of the homogeneous $TiB_2$/Cu composite and pure Cu components, respectively. Surprisingly, the YS of the SLC is not only much greater than the $\sigma_{0.2,\mathrm{ROM}}$ predicted by the ROM but also comparable to or even greater than that of homogeneous $TiB_2$/Cu composites (Fig. 5(c)). The strength increments ($\Delta\sigma_{0.2}=\sigma_{0.2}-\sigma_{0.2,\mathrm{ROM}}$) of SLC-300 °C, SLC-360 °C and SLC-420 °C are approximately 36, 88 and 51 MPa, respectively. The construction design of submicron laminates tends toward the full exploitation of the “1+1>2” mechanical performance advantage.

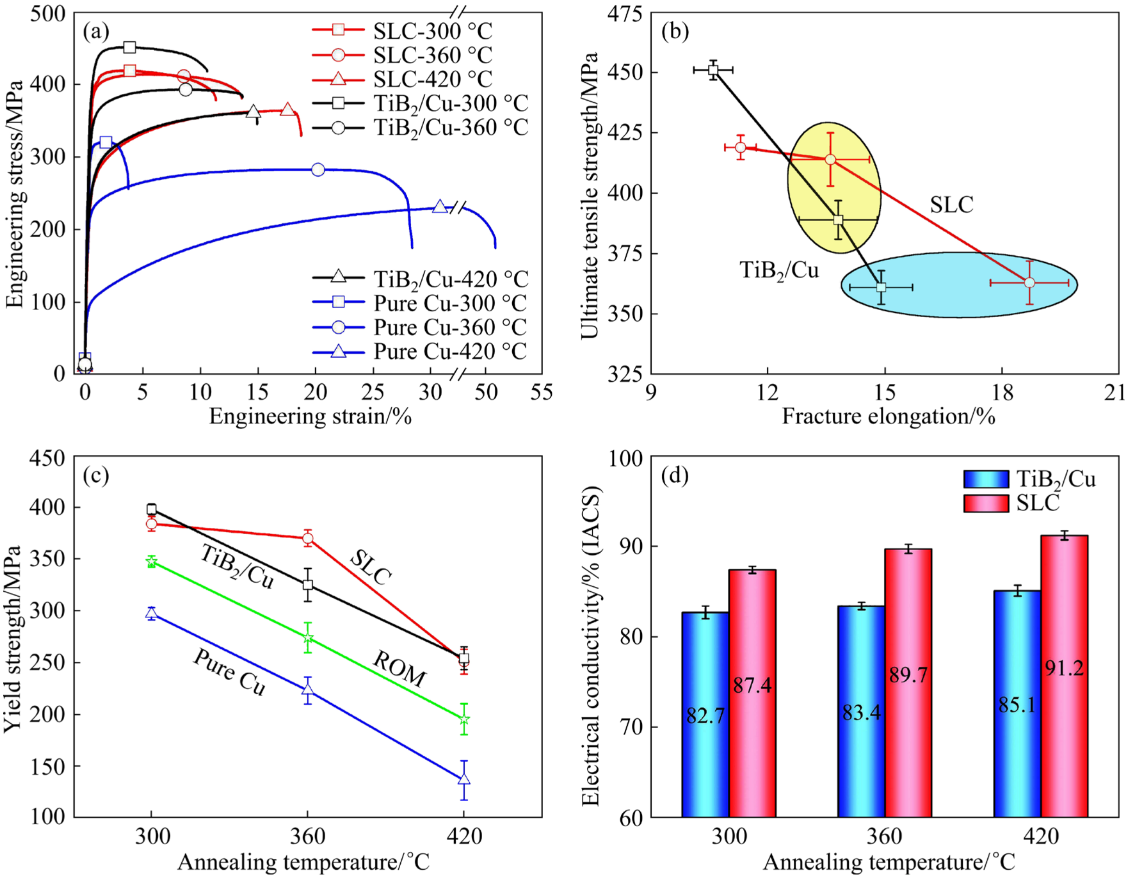

**Fig. 5** Mechanical properties and electrical conductivity of $TiB_2$/Cu−Cu SLCs, homogeneous $TiB_2$/Cu composites and pure Cu materials: (a) Engineering stress–strain curves; (b) Ultimate tensile strength versus fracture elongation; (c) Yield strength versus annealing temperature; (d) Electrical conductivity versus annealing temperature

**Table 1** Mechanical properties of samples prepared in this study

| Material | Yield strength/ MPa | Ultimate tensile strength/MPa | Fracture elongation/ % |
|---|---|---|---|
| SLC-300 °C | 384±5 | 419±7 | 11.3±0.8 |
| SLC-360 °C | 372±9 | 414±8 | 13.6±1.1 |
| SLC-420 °C | 251±6 | 363±7 | 18.7±1.0 |
| $TiB_2$/Cu-300 °C | 398±7 | 451±9 | 10.6±0.9 |
| $TiB_2$/Cu-360 °C | 325±8 | 389±11 | 13.8±0.9 |
| $TiB_2$/Cu-420 °C | 254±7 | 361±6 | 14.9±1.3 |
| Pure Cu-300 °C | 297±9 | 321±8 | 3.7±0.7 |
| Pure Cu-360 °C | 223±8 | 283±9 | 28.4±2.2 |
| Pure Cu-420 °C | 136±10 | 235±12 | 50.9±1.9 |

Figure 6 shows the relationships among the ultimate tensile strength, strengthening efficiency and electrical conductivity of the $TiB_2$ particle-reinforced Cu matrix composites. The strengthening efficiency ($\omega$) of the reinforcement was calculated via Eq. (2) [17]:

$$\omega=(\sigma_c-\sigma_m)/(V_f\sigma_m) \tag{2}$$

where $\sigma_c$ and $\sigma_m$ are the tensile strengths of the composite and the matrix, respectively; $V_f$ is the volume fraction of the reinforcement. Compared with the prepared $TiB_2$/Cu homogeneous composites and copper matrix composites reported in the literature [32−40], the SLC not only results in greater electrical conductivity without sacrificing strength, but also promotes the reinforcement and yields a higher $\omega$ (Fig. 6). Although the addition of Ti, Fe, and Cr alloying elements or $Al_2O_3$ particles helps to improve the $\omega$ of $TiB_2$/Cu composites, it always comes at the expense of electrical conductivity. In particular, with the addition of Ti alloying element, the decrease in electrical conductivity is the most significant [39,40]. The simultaneous improvement in $\omega$ and electrical conductivity can be achieved by designing submicron laminates rather than adding alloying elements or reinforcement particles.

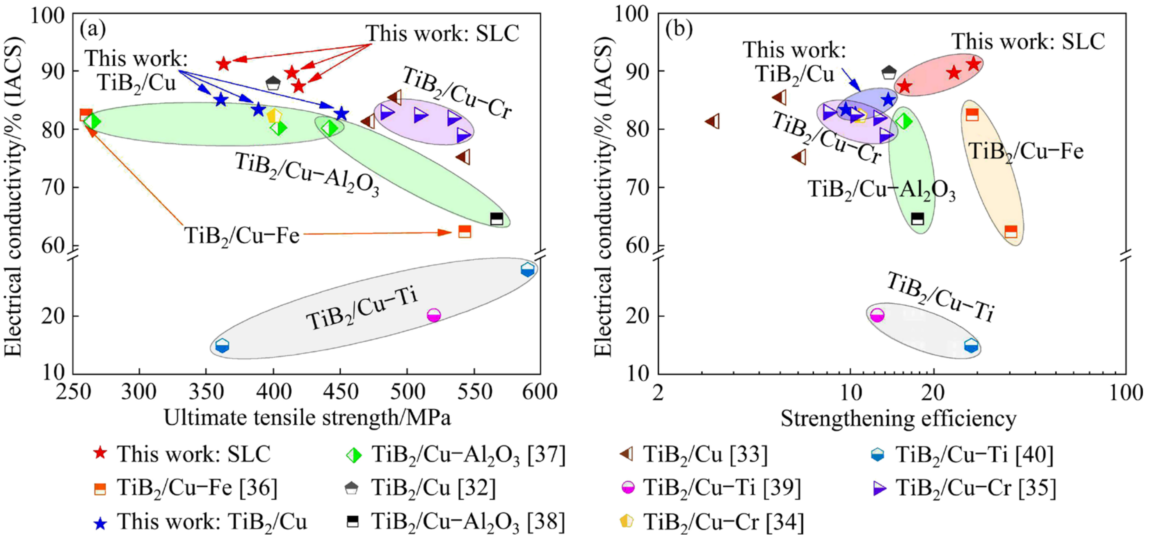

**Fig. 6** Relationships between electrical conductivity and ultimate tensile strength, and electrical conductivity and strengthening efficiency of $TiB_2$ particle-reinforced Cu matrix composites: (a) Electrical conductivity versus ultimate tensile strength; (b) Electrical conductivity versus strengthening efficiency

## 4 Discussion

### 4.1 Thermal mismatch strengthening of SLCs

The CTE of the $TiB_2$/Cu lamellae ($\mathrm{CTE}_{\mathrm{TiB_2/Cu}}$) in the SLCs is calculated via the ROM model in Eq. (3) as follows [41]:

$$\mathrm{CTE}_{\mathrm{TiB_2/Cu}}=\mathrm{CTE}_{\mathrm{TiB_2}}V_{\mathrm{TiB_2}}+\mathrm{CTE}_{\mathrm{Cu}}V_{\mathrm{Cu}} \tag{3}$$

where $\mathrm{CTE}_{\mathrm{TiB_2}}$ and $\mathrm{CTE}_{\mathrm{Cu}}$ are the CTEs of the $TiB_2$ particles ($\mathrm{CTE}_{\mathrm{TiB_2}}$=8.3×10$^{-6}$ K$^{-1}$) and the Cu matrix ($\mathrm{CTE}_{\mathrm{Cu}}$=16.6×10$^{-6}$ K$^{-1}$), respectively; $V_{\mathrm{TiB_2}}$ and $V_{\mathrm{Cu}}$ are the volume fractions of the $TiB_2$ particles ($V_{\mathrm{TiB_2}}$=3.89%) and the Cu matrix ($V_{\mathrm{Cu}}$=96.11%), respectively. Therefore, the CTE of the $TiB_2$/Cu lamellae is approximately 16.3×10$^{-6}$ K$^{-1}$, which is lower than that of the pure Cu lamellae. The difference in the CTE can lead to a normal stress effect near the $TiB_2$−Cu interface and the lamellar interface during annealing. The normal stress leads to lattice distortion and crystal misorientation in the matrix, which hinders dislocation movement and produces thermal mismatch strengthening.

Figure 7 shows the distribution of $TiB_2$ reinforcements, local misorientation and dislocation density in the SLCs after annealing at different temperatures. There are large kernel average misorientations (KAMs) and high-density dislocations in the fine-grained $TiB_2$/Cu lamellae of SLC-300 °C (black arrows in Figs. 7($a_1$−$a_3$)). However, large KAMs and high-density dislocations are present mainly in the coarse- grained pure Cu lamellae of SLC-360 °C and SLC-420 °C (pink arrows in Figs. 7($b_1$−$b_3$) and ($c_1$−$c_3$)). This finding indicates that the contribution of pure Cu lamellae to thermal mismatch strengthening is significant during annealing at relatively high temperatures. The contribution of thermal mismatch strengthening ($\sigma_{0.2,\mathrm{CTE}}$) to the YS of the SLC can be estimated via Eq. (4) [42,43]:

$$\sigma_{0.2,\mathrm{CTE}}=\beta G_{\mathrm{m}}b\sqrt{\rho_{\mathrm{a}}} \tag{4}$$

where $\beta$ is the strengthening coefficient ($\beta$=1.25), $G_{\mathrm{m}}$ is the shear modulus of the matrix ($G_{\mathrm{m}}$= 45.5 GPa), $b$ is the Burgers vector magnitude of Cu ($b$=0.255 nm), and $\rho_{\mathrm{a}}$ is the average dislocation density inside the matrix. The dislocation density ($\rho$) can be calculated via Eq. (5) [44]:

$$\rho=2\gamma/(\mu b) \tag{5}$$

where $\gamma$ is the local misorientation and $\mu$ is the unit length ($\mu$=60 nm). Therefore, the $\rho_{\mathrm{a}}$ values of SLC-300 °C, SLC-360 °C and SLC-420 °C are 1.0×10$^{15}$, 1.09×10$^{15}$ and 1.17×10$^{15}$ m$^{-2}$, respectively. Compared with those of the $TiB_2$/Cu lamellae, the average dislocation densities of the pure Cu lamellae in SLC-300 °C, SLC-360 °C and SLC-420 °C are increased by approximately −0.78×10$^{15}$, 0.59×10$^{15}$ and 0.53×10$^{15}$ m$^{-2}$, respectively. Thus, compared with homogeneous $TiB_2$/Cu composites, the additional contribution ($\Delta\sigma_{0.2,\mathrm{CTE}}$) of the thermal

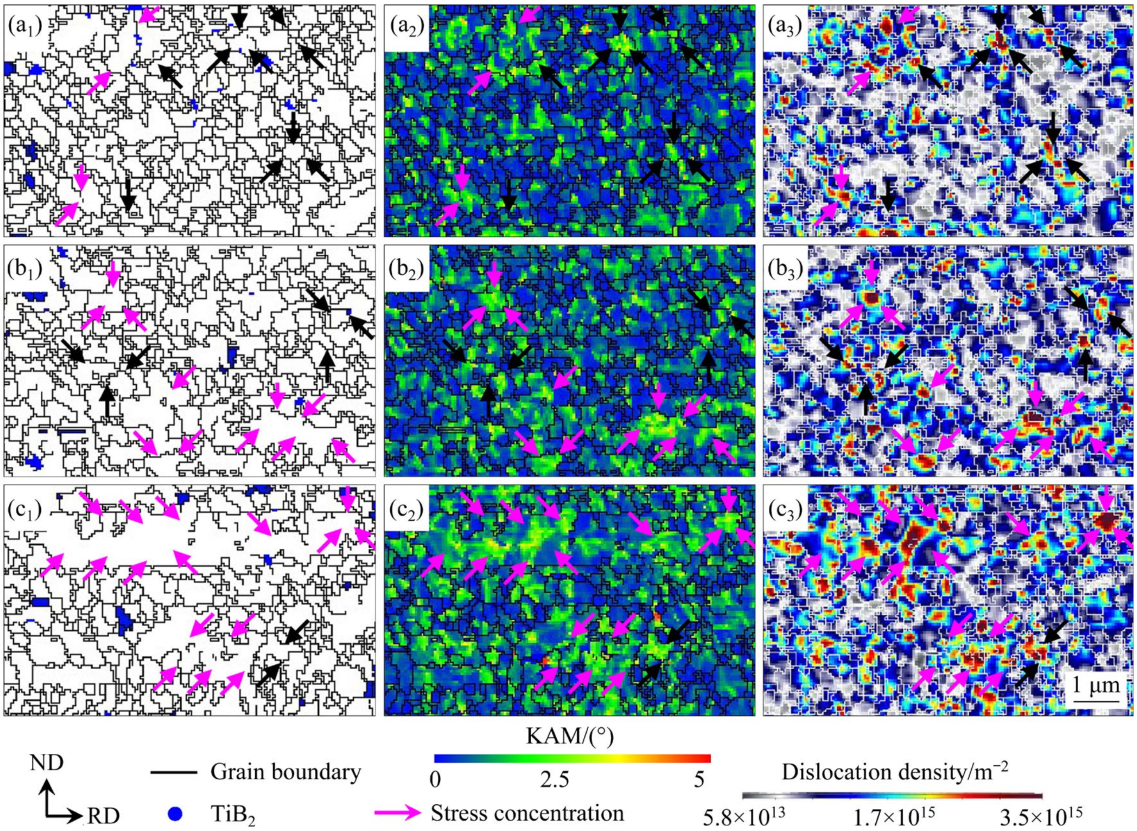

**Fig. 7** Distribution of TiB$_2$ reinforcements, local misorientation and dislocation density of SLC-300 °C (a$_1$−a$_3$), SLC-360 °C (b$_1$−b$_3$) and SLC-420 °C (c$_1$−c$_3$): (a$_1$−c$_1$) Distribution of TiB$_2$ reinforcements; (a$_2$−c$_2$) Local misorientation; (a$_3$−c$_3$) Dislocation density

mismatch strengthening of pure Cu lamellae in the SLCs to the YS can be estimated via Eq. (6):

$$\Delta\sigma_{0.2,\mathrm{CTE}}=\beta G_{\mathrm{m}} b\sqrt{\Delta\rho_{\mathrm{a}}} \tag{6}$$

where $\Delta\rho_{\mathrm{a}}$ represents the difference in the average dislocation densities of pure Cu lamellae and TiB$_2$/Cu lamellae. The calculation shows that the $\Delta\sigma_{0.2,\mathrm{CTE}}$ values of SLC-300 °C, SLC-360 °C and SLC-420 °C are approximately −36, 26 and 22 MPa, respectively. The internal stress caused by the thermal mismatch between adjacent heterogeneous lamellae is an important factor leading to the super-normal strength of SLC-360 °C and SLC-420 °C.

### 4.2 HDI strengthening and hardening of SLCs

The excellent mechanical properties of the TiB$_2$/Cu−Cu SLCs are due to the synergistic deformation mechanism between heterogeneous lamellae. The crystal orientation and substructure evolution of SLCs at different strains under uniaxial tension help to reveal the deformation behavior between heterogeneous lamellae. Figure 8 shows the crystal orientation and substructure of SLC-360 °C by the EBSD at different strains. When the strain is 14%, the pure Cu lamellae of SLC-360 °C are still equiaxed grains with high-angle grain boundaries (HAGBs, 15°<HAGBs) (Fig. 8(a$_1$)), and there are a small number of subgrains with low-angle grain boundaries (LAGBs, 2°<LAGBs<15°) (black arrows in Fig. 8(b$_1$)). The KAM near the subgrain boundary is greater (Fig. 8(c$_1$)). However, there are almost no subgrain boundaries or KAM in the fine grains of the TiB$_2$/Cu lamellae (Figs. 8(b$_1$, c$_1$)). This finding indicates that the deformation of pure Cu lamellae and TiB$_2$/Cu lamellae during uniaxial tension is not synchronized. The asynchronous deformation behavior led to the generation and accumulation of GNDs in pure Cu lamellae (Fig. 8(d$_1$)). Notably, compared with the dislocation density of SLC-360 °C without strain (Fig. 7(b$_3$)), the dislocation density during tensile deformation is significantly lower, which is mainly because the compressive residual stress caused by thermal mismatch is released soon after yielding [45]. With increasing strain, the equiaxed grains in the pure Cu

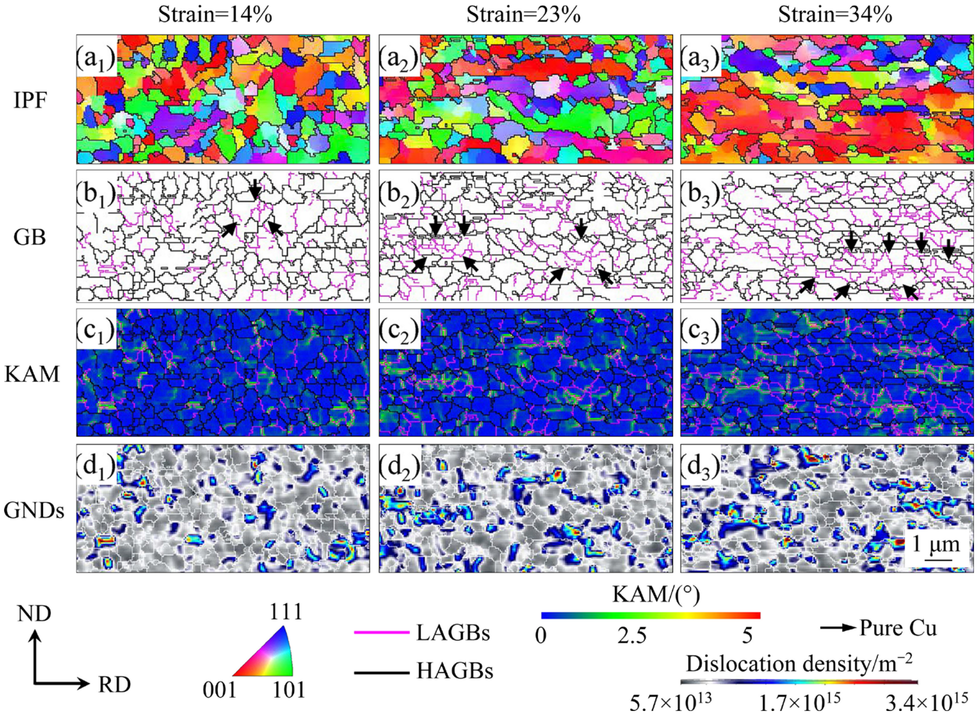

**Fig. 8** EBSD maps of SLC-360 °C at various strain levels

lamellae are gradually elongated along the tensile direction (Figs. 8($a_2$, $a_3$)), whereas the deformation of the fine grains in the $TiB_2$/Cu lamellae along the tensile direction is not significant. This is mainly related to the reinforcement particles that pin the grain boundaries in the $TiB_2$/Cu lamellae. Moreover, with increasing strain, the number of subgrain boundaries and dislocation density in the pure Cu lamellae increase (black arrows in Figs. 8($b_2$, $b_3$)), and a small number of subgrains and dislocation accumulation gradually appear in the fine grains of the $TiB_2$/Cu lamellae (Figs. 8($d_2$, $d_3$)). These findings indicate that plastic deformation of the $TiB_2$/Cu lamellae also occurs at high tensile strains. Therefore, the coarse-grained pure Cu lamellae experience greater plastic deformation, whereas the fine-grained $TiB_2$/Cu lamellae play a leading role in bearing the load. Forest dislocations and GNDs are generated during the tensile deformation of the $TiB_2$/Cu and pure Cu lamellae. Forest dislocations are a product of traditional strengthening and strain hardening. GNDs are generated to adjust the strain gradient caused by incompatible deformation [46,47], which is beneficial to generating an extra hardening effect and improving the mechanical properties of SLCs.

The improvement in the strain hardening of metal materials is closely related to the complex dislocation configurations. Figure 9 shows the TEM microstructures near the tensile fracture in SLC-360 °C, which finely characterizes the evolution of the dislocation configuration between the $TiB_2$/Cu lamellae and pure Cu lamellae. Compared with that of SLC-360 °C without strain (Fig. 9(a)), there is a gradient change in the GND near the lamellar interface in the pure Cu lamellae at a small strain (Fig. 9(b)), which is the result of incompatible deformation between the $TiB_2$/Cu lamellae and the pure Cu lamellae. Because of the higher Schmid factor and preferentially activated intragranular slip, the coarse-grained pure Cu lamellae deform before the fine-grained $TiB_2$/Cu lamellae deform. This incompatible deformation needs to be adjusted by GNDs, which contributes to extra strain hardening [48,49]. GNDs accumulate near the lamellar interface in pure Cu lamellae and exhibit a gradient decrease in density (Fig. 9(b)), which confirms that the slip strain in pure Cu lamellae gradually decreases with increasing distance from the lamellar interface. Moreover, dislocations are also generated and accumulate at the twin boundaries (Fig. 9(c)), which is a typical manifestation of twin-enhanced strain hardening in traditional Cu materials [50,51]. The lamellar interface acts as an effective barrier for GNDs and slip dislocations, which helps to increase the local

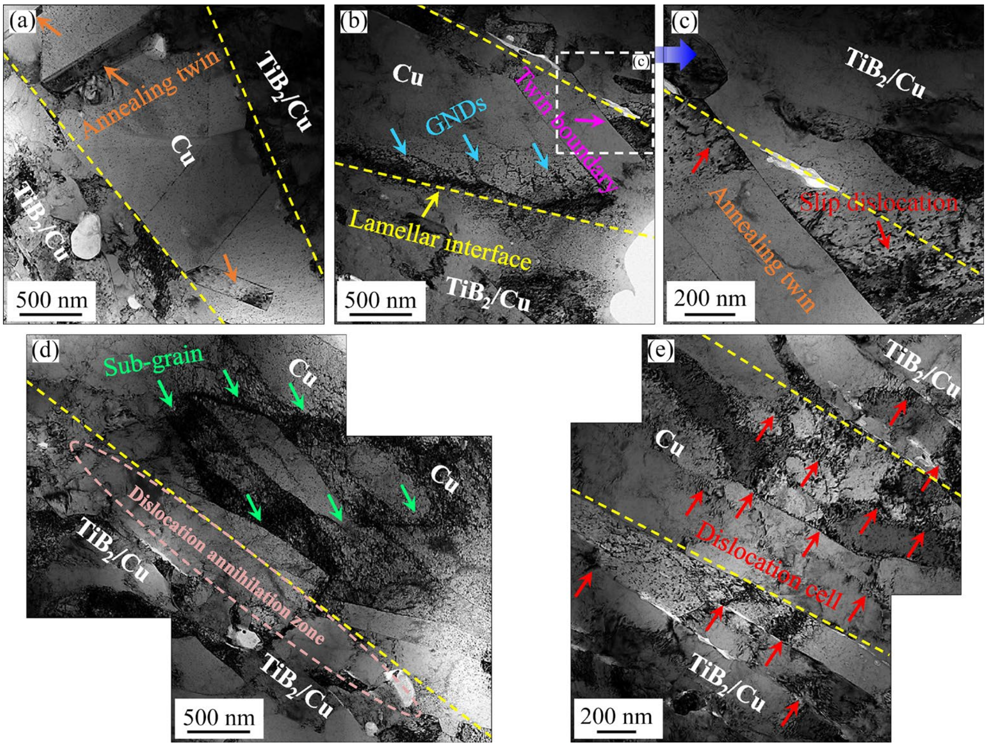

**Fig. 9** TEM images near tensile fracture in SLC-360 °C: (a) Laminated microstructure without tensile strain; (b) Accumulation and gradient distribution of GNDs near lamellar interface; (c) Enlarged microstructure of white-dotted rectangle in (b); (d) Formation of subgrains and occurrence of disentanglement and annihilation of existing dislocations; (e) Distribution of dislocation cells

strength. At a higher strain, the equiaxed grains and twins in the Cu lamellae disappear, and many subgrains caused by dislocation entanglement are formed (Fig. 9(d)). The dislocation density at the subgrain boundaries is greater, whereas the dislocation density inside the subgrain boundaries is lower. This confirms the activation of a large number of intragranular slip events in pure Cu lamellae. Therefore, the contribution of the interface plasticity in pure Cu lamellae gradually decreases with loading. Moreover, disentanglement and annihilation of existing dislocations occur near the lamellar interface in the $TiB_2/Cu$ lamellae (Fig. 9(d)), which contribute to the toughening of the $TiB_2/Cu$ lamellae. In the high-strain stage, the multiple slip events of a large number of dislocations make it difficult to distinguish between grain boundaries in pure Cu lamellae, and dislocation cells develop well (Fig. 9(e)), which proves that dislocation slip in pure Cu lamellae prolongs plastic deformation. Moreover, many dislocation cells reappear near the lamellar interface in the $TiB_2/Cu$ lamellae, which is the result of the partial recovery of forest hardening during tensile deformation [52,53].

The extra strengthening caused by the incompatible deformation in the $TiB_2/Cu$−Cu SLCs can be estimated through loading–unloading–reloading (LUR) tests. Figure 10(a) shows the results of LUR tests on the SLC. The remarkable mechanical hysteresis loop indicates that the SLC exhibits Bauschinger effect during the tensile deformation (Fig. 10(b)), which contributes to the generation of extra HDI stress. The mechanical hysteresis loop of SLC-360 °C is the largest, indicating that it produces the strongest Bauschinger effect and the highest HDI stress. The extra HDI stress ($\sigma_{HDI}$) of the SLC is calculated via Eq. (7) (Fig. 10(c)):

$$\sigma_{HDI}=(\sigma_r+\sigma_u)/2 \tag{7}$$

where $\sigma_r$ and $\sigma_u$ are the reloading and unloading yield stresses, respectively. Based on the yield strain in Fig. 10(a) and the growth rate of HDI stress with strain in Fig. 10(c), the contribution of HDI stress to the YS ($\Delta\sigma_{0.2,HDI}$) of the SLC was predicted (inset in Fig. 10(c)). The $\Delta\sigma_{0.2,HDI}$ values of SLC-300 °C, SLC-360 °C and SLC-420 °C are

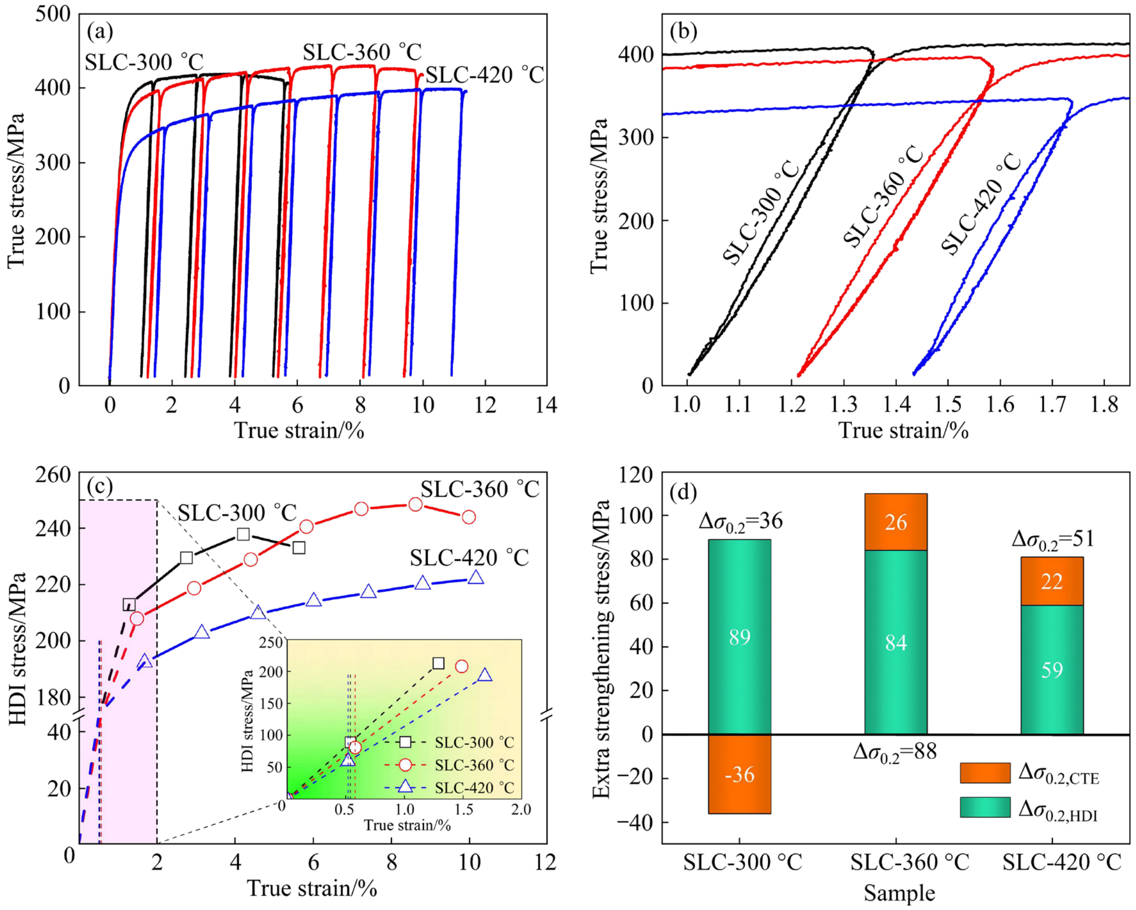

**Fig. 10** Bauschinger effect and HDI stress of SLCs: (a) Stress–strain curves of SLCs in LUR tests; (b) 1st enlarged hysteresis loops of (a); (c) Change in HDI stress with increasing applied true strain; (d) Contribution of extra strengthening stress to YS of SLCs

89, 84 and 59 MPa, respectively (Fig. 10(d)). The extra strengthening ($\Delta\sigma_{0.2}$) of the SLC is lower than the sum of $\Delta\sigma_{0.2,\mathrm{CTE}}$ and $\Delta\sigma_{0.2,\mathrm{HDI}}$ (Fig. 10(d)). This is mainly because the YS of composite materials usually results from grain refinement strengthening ($\sigma_{0.2,\mathrm{Hall-Petch}}$), dislocation strengthening due to differences in the coefficients of thermal expansion ($\sigma_{0.2,\mathrm{CTE}}$), load transfer strengthening ($\sigma_{0.2,\mathrm{Load}}$) and Orowan strengthening ($\sigma_{0.2,\mathrm{Orowan}}$) [30]. The coarse-grained pure Cu lamellae of the SLC reduce $\sigma_{0.2,\mathrm{Hall-Petch}}$, $\sigma_{0.2,\mathrm{Load}}$ and $\sigma_{0.2,\mathrm{Orowan}}$. In particular, the decrease in $\sigma_{0.2,\mathrm{Hall-Petch}}$ is the most significant, which is due to the obvious grain coarsening of pure Cu lamellae caused by the increase in annealing temperature (Fig. 2).

### 4.3 Fracture characteristics of SLCs

The fracture characteristics in the uniaxial tensile process are helpful for revealing the toughening mechanism of $TiB_2$/Cu−Cu SLCs. Figure 11 shows the crack propagation and fracture morphology of the SLCs. Both SLC-360 °C and SLC-420 °C exhibit mainly crack deflection (Figs. 11($a_1$, $b_1$)), which is caused by the uneven distribution of strain between the $TiB_2$/Cu lamellae and pure Cu lamellae. Many discrete microcracks, delamination cracks and tunnel cracks are found in the $TiB_2$/Cu lamellae (Figs. 11($a_2$, $b_2$)). Microcracks exist near the $TiB_2$ particle interface, which are attributed to the stress concentration caused by the dislocation pile-up near the particle interface. Discrete microcracks help to alleviate the stress concentration around the particle interface and delay the initiation of cracks and the propagation of main cracks. Delamination cracks are parallel to the lamellar interface, which are the result of incompatible deformation between adjacent heterogeneous component lamellae in a coordinated manner perpendicular to the tensile direction. Delamination cracks promote the bifurcation of the main crack and reduce its propagation rate. The tunnel cracks are the result of the further propagation

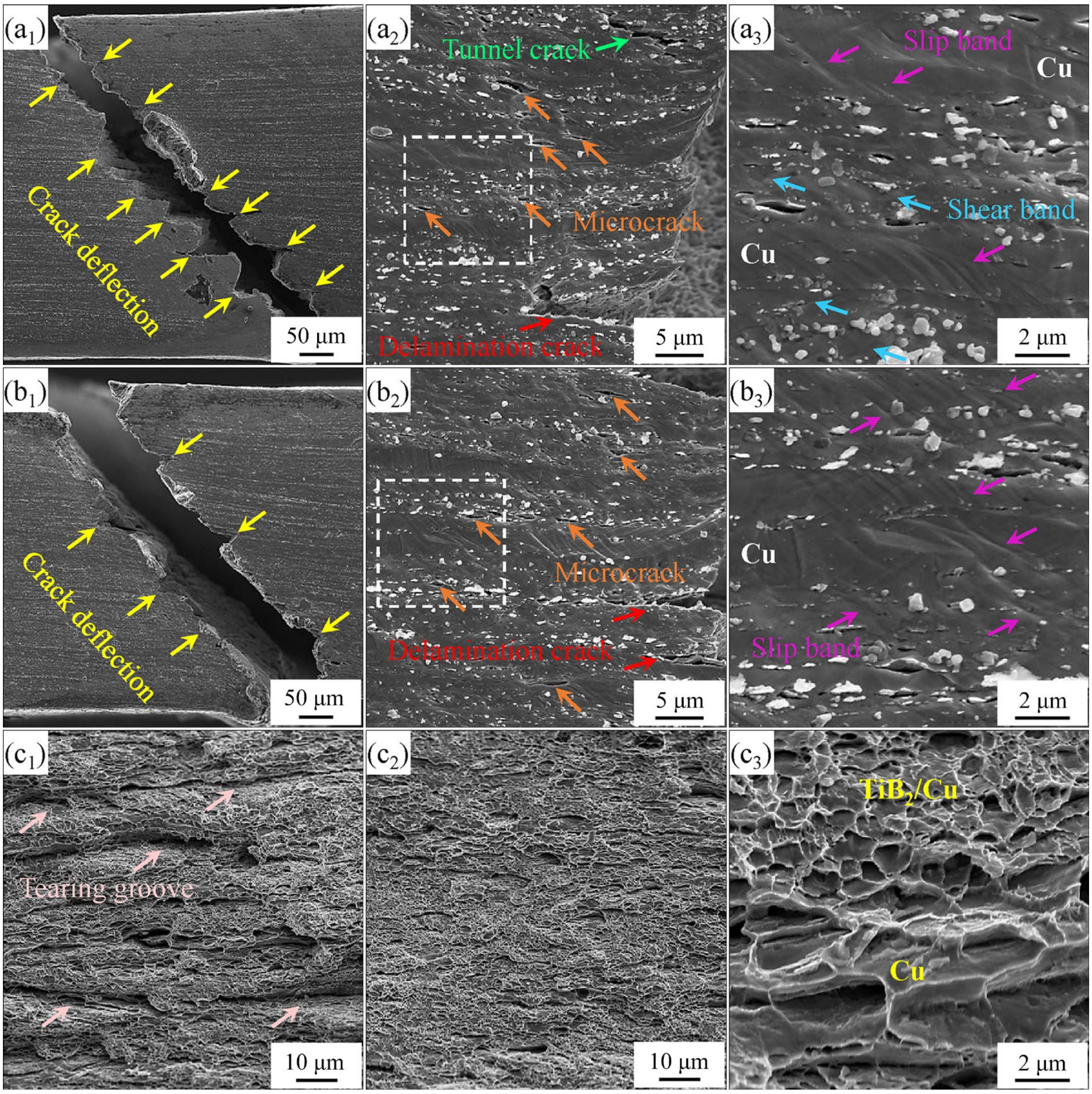

**Fig. 11** Tensile fracture characteristics of SLCs: (a1) Tensile fracture cross-sectional microstructure of SLC-360 °C; (a2) Microstructure near fracture in (a1); (a3) Enlarged microstructure of white dotted rectangle in (a2); (b1) Tensile fracture cross-sectional microstructure of SLC-420 °C; (b2) Microstructure near fracture in (b1); (b3) Enlarged microstructure of white dotted rectangle in (b2); (c1, c2) Tensile fracture morphologies of SLC-360 °C and SLC-420 °C, respectively; (c3) Local enlarged microstructure in (c1)

and interconnection of discrete microcracks, which penetrate into the $TiB_2$/Cu lamellae and terminate at the lamellar interface because of the passivation of their tips by the adjacent high-plasticity pure Cu lamellae. The blunting of tunnel crack tips confirms the important role of pure Cu lamellae in the synergistic deformation of low-plasticity $TiB_2$/Cu lamellae. However, no microcracks are found in the pure Cu lamellae. The ubiquitous slip bands in pure Cu lamellae indicate uniform plastic deformation caused by dislocation slip (Figs. 11(a3, b3)). The results indicate that the pure Cu lamellae experience severer tensile deformation, which is consistent with the EBSD (Fig. 8) and TEM (Fig. 9) results. There are many unstable shear bands in the $TiB_2$/Cu lamellae of SLC-360 °C (Fig. 11(a3)), indicating that the dislocation activity in the $TiB_2$/Cu lamellae is limited and difficult to release. The existence of shear bands confirms the strain localization in the $TiB_2$/Cu lamellae. The main slip bands in the $TiB_2$/Cu lamellae and pure Cu lamellae of SLC-420 °C are consistent, which indicates sufficient activity of the dislocations and weak strain localization in the $TiB_2$/Cu lamellae. Moreover, many tearing grooves are present in the fracture morphology of the $TiB_2$/Cu lamellae in SLC-360 °C

(Fig. 11($c_1$)), whereas the fracture morphology of SLC-420 °C is smoother (Fig. 11($c_2$)). This indicates that there are greater incompatibility deformation and stronger interface constraint effect between adjacent heterogeneous lamellae of SLC-360 °C, which is consistent with the stronger Bauschinger effect and higher HDI stress observed in the LUR test results (Fig. 10). In addition, the fracture morphologies of SLC-360 °C and SLC-420 °C are alternately distributed with small and large dimples (Figs. 11($c_1$, $c_2$)). There are no defects, such as debonding or cracking at the lamellar interface, which confirms good bonding between the $TiB_2$/Cu lamellae and pure Cu lamellae. The well-bonded lamellar interface ensures the stable and persistent generation of HDI stress [54].

For homogeneous $TiB_2$/Cu composites [55,56], cracks usually appear in the low-strain shear region, and there is only a single microcrack at the $TiB_2$ particle interface, which leads to very limited fracture toughness. In contrast, for the main crack deflection fracture, many discrete microcracks, delamination cracks and tunnel cracks were observed during tensile deformation of the SLCs, which indicated that the strain-induced cracks played a lasting role in strain regulation during the whole deformation process. The interaction and propagation of multimode cracks are the main method of damage accumulation, especially when the plastic deformation capacity is exhausted, which can significantly improve the fracture toughness of composites [57,58].

In summary, the advantage of SLCs in balancing mechanical properties and electrical conductivity lies in the structural effect of heterogeneous microstructures (Fig. 12). The thickness of pure Cu lamellae with a developed slip system in SLCs is only submicron structure, which results in interactions between GNDs and statistically stored dislocations (SSDs). The interaction of dislocations is beneficial to improving the storage rate of dislocations and the work hardening ability of SLCs. Moreover, the submicron laminated configuration provides external toughening for SLCs through the synergy between multiple crack propagation modes. In addition, according to Matthiessen's law, the pure Cu lamellae with low grain boundary scattering resistance, low dislocation scattering resistance and no $TiB_2$ particle interface scattering resistance provide the conditions for the rapid transport of carriers, and the close interface between the $TiB_2$/Cu lamellae and the pure Cu lamellae can minimize the interfacial impedance stemming from electron-boundary scattering alongside the lamellar interface. Therefore, SLCs achieve a significant improvement in electrical conductivity while obtaining mechanical properties of "1 + 1 > 2".

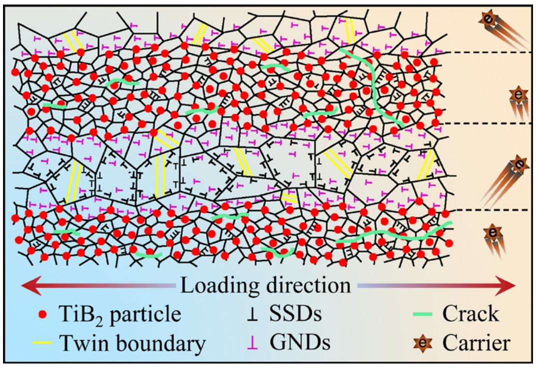

**Fig. 12** Schematic illustration of dislocation behavior, crack propagation and carrier transport in SLCs

## 5 Conclusions

(1) The as-prepared $TiB_2$/Cu−Cu laminated composites have an alternating heterogeneous structure of fine-grained $TiB_2$/Cu lamellae and coarse-grained Cu lamellae. The thickness of a single-component lamella is approximately several hundred nanometers, and the $TiB_2$–Cu interface and lamellar interface are firmly bonded.

(2) The difference in the CTEs of the $TiB_2$/Cu and Cu lamellae is beneficial to thermal mismatch strengthening. Moreover, a lamellar thickness of submicrons promotes the interaction between GNDs and SSDs, which significantly improves the mechanical properties of SLCs.

(3) The interaction and propagation of multimode cracks provide extrinsic toughening for SLCs. In addition, pure Cu lamellae with low electron scattering resistance provide a channel for the rapid transport of carriers, which ensures the high electrical conductivity of SLCs.

### CRediT authorship contribution statement

**Fei HAN:** Conceptualization, Writing − Original draft preparation, Writing − Review and editing; **Yi-hui JIANG:** Project administration, Funding acquisition, Writing − Review and editing; **Fei CAO:** Formal analysis, Data curation; **Hao SHI:** Investigation;

**Lei CAI:** Investigation; **Shu-hua LIANG:** Project administration, Funding acquisition, Writing − Review and editing.

## Declaration of competing interest

The authors declare that they have no known competing financial interests or personal relationships that could have appeared to influence the work reported in this paper.

## Acknowledgments

This work was supported by the National Natural Science Foundation of China (Nos. 52127802, 52322409, 52271137), the Scientific Research Program of Education Department of Shaanxi Province, China (No. 22JY050), and the Science and Technology Project of Xi'an, China (No. 2021SFGX0004).

## References

[1] LI W, YANG Y, LIU J, ZHOU Y, LI M, WEN S F, WEI Q S, YAN C Z, SHI Y S. Enhanced nanohardness and new insights into texture evolution and phase transformation of TiAl/$TiB_2$ in-situ metal matrix composites prepared via selective laser melting [J]. Acta Materialia, 2017, 136: 90−104.

[2] KARTHISELVA N S, BAKSHI S R. Carbon nanotube and in-situ titanium carbide reinforced titanium diboride matrix composites synthesized by reactive spark plasma sintering [J]. Materials Science and Engineering: A, 2016, 663: 38−48.

[3] GOSSLAR D, GÜNTHER R, HECHT U, HARTIG C, BORMANN R. Grain refinement of TiAl-based alloys: The role of $TiB_2$ crystallography and growth [J]. Acta Materialia, 2010, 58: 6744−6751.

[4] LI Y F, XIAO B, WANG G L, SUN L, ZHENG Q L, LIU Z W, GAO Y M. Revealing the novel fracture mechanism of the interfaces of $TiB_2$/Fe composite from a first principles investigation [J]. Acta Materialia, 2018, 156: 228−244.

[5] XIAO Peng, GAO Yi-min, YANG Cui-cui, LI Ye-fei, HUANG Xiao-yu, LIU Qing-kun, ZHAO Si-yong, XU Fei-xing, MANOJ G. Strengthening and toughening mechanisms of Mg matrix composites reinforced with specific spatial arrangement of in-situ $TiB_2$ nanoparticles [J]. Composites: Part B, 2020, 198: 108174.

[6] ASKARPOUR M, SADEGHIAN Z, REIHANIAN M. Role of powder preparation route on microstructure and mechanical properties of Al−$TiB_2$ composites fabricated by accumulative roll bonding (ARB) [J]. Materials Science and Engineering: A, 2016, 677: 400−410.

[7] GUO Ming-xing, SHEN Kun, WANG Ming-pu. Relationship between microstructure, properties and reaction conditions for Cu−$TiB_2$ alloys prepared by in situ reaction [J]. Acta Materialia, 2009, 57: 4568−4579.

[8] YU Zhu-li, ZHU He-guo, HUANG Jie-wen, LI Jian-liang, XIE Zong-han. Processing and characterization of in-situ ultrafine $TiB_2$−Cu composites from Ti−B−Cu system [J]. Powder Technology, 2017, 320: 66−72.

[9] LI Zi-li, WANG Wei-min, WANG Ji-lin. Effects of $TiB_2$ on microstructure of nano-grained Cu−Cr−$TiB_2$ composite powders prepared by mechanical alloying [J]. Advanced Powder Technology, 2014, 25: 415−422.

[10] LU L, SHEN Y F, CHEN X H, QIAN L H, LU K. Ultrahigh strength and high electrical conductivity in copper [J]. Science, 2004, 304: 422−426.

[11] LU K. The future of metals [J]. Science, 2010, 328: 319−320.

[12] ZHANG Xue-hui, LI Xiao-xian, CHEN Hao, LI Tian-bai, SU Wei, GUO Sheng-da. Investigation on microstructure and properties of Cu−$Al_2O_3$ composites fabricated by a novel in-situ reactive synthesis [J]. Materials & Design, 2016, 92: 58−63.

[13] CAO Fei, DONG Ge-zhi, JIANG Yi-hui, XIAO Peng, WANG Tong-min, LIANG Shu-hua. Effect of La addition on microstructures and properties of $TiB_2$(-TiB)/Cu hybrid composites fabricated by in-situ reaction [J]. Materials Science and Engineering: A, 2020, 789: 139605.

[14] JIANG Yi-hui, WANG Ding-wen, XU Ying-qin, CAO Fei, LIANG Shu-hua. Fabrication and properties of in situ heterogeneous Cu/$TiB_2$ composites with a harmonic structure [J]. Materials Letters, 2020, 263: 127032.

[15] WANG Tong-min, ZOU Cun-lei, CHEN Zong-ning, LI Ming-yu, WANG Wei, LI Ren-geng, KANG Hui-jun. In situ synthesis of $TiB_2$ particulate reinforced copper matrix composite with a rotating magnetic field [J]. Materials & Design, 2015, 65: 280−288.

[16] LÓPEZ M, CORREDOR D, CAMURRI C, VERGARA V, JIMÉNEZ J. Performance and characterization of dispersion strengthened Cu−$TiB_2$ composite for electrical use [J]. Materials Characterization, 2005, 55: 252−262.

[17] CAO Mu, XIONG Ding-bang, TAN Zhan-qiu, JI Gang, AMIN-AHMADI B, GUO Qiang, FAN Gen-lian, GUO Cui-ping, LI Zhi-qiang, ZHANG Di. Aligning graphene in bulk copper: Nacre-inspired nanolaminated architecture coupled with in-situ processing for enhanced mechanical properties and high electrical conductivity [J]. Carbon, 2017, 117: 65−74.

[18] HAN Fei, JIANG Yi-hui, CAO Fei, CAI Lei, LIANG Shu-hua. A hard/soft layered micro-structured CuCrZr alloy with strength, ductility and electrical conductivity synergy [J]. Materials Characterization, 2023, 199: 112836.

[19] DING C G, XU J, SHAN D B, GUO B, LANGDON T G. Sustainable fabrication of Cu/Nb composites with continuous laminated structure to achieve ultrahigh strength and excellent electrical conductivity [J]. Composites: Part B, 2021, 211: 108662.

[20] HUANG C X, WANG Y F, MA X L, YIN S, HÖPPEL H W, GÖKEN M, WU X L, GAO H J, ZHU Y T. Interface affected zone for optimal strength and ductility in heterogeneous laminate [J]. Materials Today, 2018, 21: 713−719.

[21] HAN Fei, JIANG Yi-hui, CAO Fei, CAI Lei, ZHANG Han-xiao, LIANG Shu-hua. Role of gradient heterogeneous interfaces in synergetic strengthening and toughening of

layered CuCrZr/Cu composites [J]. Materials Science and Engineering: A, 2023, 885: 145613.

[22] MA X L, HUANG C X, MOERING J, RUPPERT M, HÖPPEL H W, GÖKEN M, NARAYAN J, ZHU Y T. Mechanical properties of copper/bronze laminates: Role of interfaces [J]. Acta Materialia, 2016, 116: 43−52.

[23] JIANG Yi-hui, WANG Chen, LIANG Shu-hua, REN Jian-qiang, DU Xiang, LIU Feng. TiB$_2$(-TiB)/Cu in-situ composites prepared by hot-press with the sintering temperature just beneath the melting point of copper [J]. Materials Characterization, 2016, 121: 76−81.

[24] LIU L, LI S F, PAN D, HUI D X, ZHANG X, LI B, LIANG T S, SHI P P, BAHADOR A, UMEDA J, KONDOH K, LI S L, GAO L N, WANG Z M, LI G, ZHANG S Y, WANG R H, CHEN W G. Loss-free tensile ductility of dual-structure titanium composites via an interdiffusion and self-organization strategy [J]. Proceedings of the National Academy of Sciences of the United States of America, 2023, 120: e2302234120.

[25] CHEN Jia-jing, HAN Yuan-fei, LI Shao-peng, WEI Zi-chao, LE Jian-wen, SHI Hui-gang, HUANG Guang-fa, LU Wei-jie, ZHANG Di. Evading the strength and ductility trade-off dilemma in titanium matrix composites through designing bimodal grains and micro-nano reinforcements [J]. Scripta Materialia, 2023, 235: 115625.

[26] ZHANG Xing-de, JIANG Yi-hui, CAO Fei, YANG Tian, GAO Fan, LIANG Shu-hua. Hybrid effect on mechanical properties and high-temperature performance of copper matrix composite reinforced with micro-nano dual-scale particles [J]. Journal of Materials Science & Technology, 2024, 172: 94−103.

[27] HUANG M, XU C, FAN G H, MAAWAD E, GAN W M, GENG L, LIN F X, TANG G Z, WU H, DU Y, LI D Y, MIAO K S, ZHANG T T, YANG X S, XIA Y P, CAO G J, KANG H J, WANG T M, XIAO T Q, XIE H L. Role of layered structure in ductility improvement of layered Ti−Al metal composite [J]. Acta Materialia, 2018, 153: 235−249.

[28] MA X L, HUANG C X, XU W Z, ZHOU H, WU X L, ZHU Y T. Strain hardening and ductility in a coarse-grain/nanostructure laminate material [J]. Scripta Materialia, 2015, 103: 57−60.

[29] AJANTIWALAY T, MA X L, YU A Q, POLE M, SILVERSTEIN J, MATHAUDHU S, DEVARAJ A, GWALANI B. Shear deformation of pure-Cu and Cu/Nb nano-laminates using micromechanical testing [J]. Scripta Materialia, 2023, 230: 115403.

[30] XIAO Peng, ZHAO Qi-qiang, SHENG Yu-peng, YANG Cui-cui, GAO Yi-min, WU Wen-yu, LIU Zhi-wei, YI Yan-liang. Superior strength-toughness synergy of heterogeneous TiB$_{2\mathrm{p}}$/AZ91 composites containing hard/soft zones via tailoring bimodal grain structure [J]. Materials Science and Engineering: A, 2023, 887: 145775.

[31] WANG L D, XUE Z W, QIAO Y J, FEI W D. Anisotropic thermal expansion behaviors of copper matrix in $\beta$-eucryptite/copper composite [J]. Materials Science and Engineering: B, 2012, 177: 873−876.

[32] SHI Hao, CAO Fei, ZHANG Hai-dong, WANG Tong-le, GAO Huai-bao, WEN Bin-bin, ZOU Jun-tao, JIANG Yi-hui, LIANG Shu-hua. Densification behavior, mechanical and electrical properties of in-situ TiB$_{2\mathrm{p}}$/Cu composite powder via vacuum hot pressing [J]. Materials Characterization, 2023, 202: 113004.

[33] LIANG Shu-hua, LI Wei-zhen, JIANG Yi-hui, CAO Fei, DONG Ge-zhi, XIAO Peng. Microstructures and properties of hybrid copper matrix composites reinforced by TiB whiskers and TiB$_2$ particles [J]. Journal of Alloys and Compounds, 2019, 797: 589−594.

[34] FENG Jiang, SONG Ke-xing, LIANG Shu-hua, GUO Xiu-hua, JIANG Yi-hui. Electrical wear of TiB$_2$ particle-reinforced Cu and Cu−Cr composites prepared by vacuum arc melting [J]. Vacuum, 2020, 175: 109295.

[35] ZHANG Peng-chao, JIE Jin-chuan, GAO Yuan, LI Hang, CAO Zhi-qiang, WANG Tong-min, LI Ting-ju. Preparation and properties of TiB$_2$ particles reinforced Cu−Cr matrix composite [J]. Materials Science and Engineering: A, 2015, 642: 398−405.

[36] PAN S H, ZHENG T Q, YAO G C, CHI Y T, ROSA I D, LI X C. High-strength and high-conductivity in situ Cu−TiB$_2$ nanocomposites [J]. Materials Science and Engineering: A, 2022, 831: 141952.

[37] CHEN Wei, GAO Gui-juan, MENG Xiang-peng, ZHAO Xiao-jun, JIANG Yan-bin, WANG Meng, LI Zhou, XIAO Lai-rong. Microstructure, properties and strengthening mechanism of Cu−TiB$_2$−Al$_2$O$_3$ composite prepared by liquid phase in-situ reaction casting [J]. Journal of Alloys and Compounds, 2022, 912: 165170.

[38] ZHOU Tao, CHEN Wei, JIANG Yan-bin, QIU Wen-ting, CHEN Cai, XIAO Xu, QIN Liu-xin, GONG Shen, JIA Yan-lin, LI Zhou. Microstructure, properties and reaction kinetics of a Cu−Al$_2$O$_3$−TiB$_2$ alloy prepared by a new liquid phase in-situ reaction technology [J]. Journal of Materials Research & Technology, 2023, 26: 4024−4041.

[39] CHEN Dan, JIANG Yi-hui, LI Yu-fa, LIU Di, HE Jiang-tan, CAO Fei, LIANG Shu-hua. In situ TiB$_2$/Cu composites fabricated by spray deposition using solid−liquid and liquid−liquid reactions [J]. Transactions of Nonferrous Metals Society of China, 2020, 30: 1849−1856.

[40] SOBHANI M, MIRHABIBI A, ARABI H, BRYDSON R M D. Effects of in situ formation of TiB$_2$ particles on age hardening behavior of Cu−1wt.%Ti−1wt.%TiB$_2$ [J]. Materials Science and Engineering: A, 2013, 577: 16−22.

[41] ZHANG L, QU X H, HE X B, DUAN B H, REN S B, QIN M L. Thermo-physical and mechanical properties of high volume fraction SiC$_\mathrm{p}$/Cu composites prepared by pressureless infiltration [J]. Materials Science and Engineering: A, 2008, 489: 285−293.

[42] SAHOO B N, PANIGRAHI S K. Synthesis, characterization and mechanical properties of in-situ (TiC−TiB$_2$) reinforced magnesium matrix composite [J]. Materials & Design, 2016, 109: 300−313.

[43] XIAO Peng, GAO Yi-min, YANG Cui-cui, LIU Zhi-wei, LI Ye-fei, XU Fei-xing. Microstructure, mechanical properties and strengthening mechanisms of Mg matrix composites reinforced with in situ nanosized TiB$_2$ particles [J]. Materials Science and Engineering: A, 2018, 710: 251−259.

[44] KUBIN L P, MORTENSEN A. Geometrically necessary dislocations and strain-gradient plasticity: A few critical issues [J]. Scripta Materialia, 2003, 48: 119−125.

[45] WU Xiao-lei, ZHU Yun-tian, LU Ke. Ductility and strain hardening in gradient and lamellar structured materials [J]. Scripta Materialia, 2020, 186: 321−325.

[46] WANG Yan-fei, WEI Yue-guang, ZHAO Zhi-fu, LONG Hao, LIN Zhong-ya, GUO Feng-jiao, HE Qiong, HUANG Chong-xiang, ZHU Yun-tian. Activating dispersed strain bands in tensioned nanostructure layer for high ductility: The effects of microstructure inhomogeneity [J]. International Journal of Plasticity, 2022, 149: 103159.

[47] YANG T, ZHAO Y L, TONG Y, JIAO Z B, WEI J, CAI J X, HAN X D, CHEN D, HU A, KAI J J, LU K, LIU Y, LIU C T. Multicomponent intermetallic nanoparticles and superb mechanical behaviors of complex alloys [J]. Science, 2018, 362: 933−937.

[48] WU Xiao-lei, ZHU Yun-tian. Heterogeneous materials: A new class of materials with unprecedented mechanical properties [J]. Materials Research Letters, 2017, 5: 527−532.

[49] ZHU Yun-tian, WU Xiao-lei. Perspective on hetero-deformation induced (HDI) hardening and back stress [J]. Materials Research Letters, 2019, 7: 393−398.

[50] WANG Yin-min, CHEN Ming-wei, ZHOU Feng-hua, MA En. High tensile ductility in a nanostructured metal [J]. Nature, 2002, 419: 912−915.

[51] SANSOZ F, LU K, ZHU T, MISRA A. Strengthening and plasticity in nanotwinned metals [J]. Materials Research Society Bulletin, 2016, 41: 292−297.

[52] WU Xiao-lei, JIANG Ping, CHEN Liu, YUAN Fu-ping, ZHU Yun-tian. Extraordinary strain hardening by gradient structure [J]. Proceedings of the National Academy of Sciences of the United States of America, 2014, 111: 7197−7201.

[53] YUAN Fu-ping, YAN Ding-shun, SUN Jiang-da, ZHOU Ling-ling, ZHU Yun-tian, WU Xiao-lei. Ductility by shear band delocalization in the nano-layer of gradient structure [J]. Materials Research Letters, 2019, 7: 12−17.

[54] HAN Fei, JIANG Yi-hui, CAO Fei, HAN Le, ZHU Jia-lin, WANG Wei, LIANG Shu-hua. Enhanced strength, ductility and electrical conductivity of CuCrZr alloys by tailoring a heterogeneous layered microstructure [J]. Materials Science and Engineering: A, 2023, 863: 144502.

[55] CAO Fei, ZHANG Xing-de, JIANG Yi-hui, CAI Peng-tao, LI Qian, WANG Tong-min, DONG Ge-zhi, GAO Fan, LIANG Shu-hua. Effect of different rare earths on microstructures and tensile strength of in situ hybrid reinforced ($TiB_{2p}$+$TiB_w$)/Cu composites [J]. Materials Characterization, 2022, 184: 111624.

[56] SHI Hao, CAO Fei, WANG Tong-le, ZHANG Hai-dong, GAO Huai-bao, LIU Hao-tian, GAO Lei, ZOU Jun-tao, JIANG Yi-hui, LIANG Shu-hua. A well-balanced strength and electrical conductivity in rolled composite prepared by in-situ $TiB_{2p}$/Cu composite powder [J]. Journal of Materials Research and Technology, 2023, 27: 1−10.

[57] PHILLION A B, COCKCROFT S L, LEE P D. X-ray micro-tomographic observations of 367 hot tear damage in an Al−Mg commercial alloy [J]. Scripta Materialia, 2006, 55: 489−492.

[58] WU Hao, FAN Guo-hua, HUANG Meng, GENG Lin, CUI Xi-ping, CHEN Rong-chang, PENG Guan-yun. Fracture behavior and strain evolution of laminated composites [J]. Composite Structures, 2017, 163: 123−128.

# 采用亚微米叠层结构同时提高 $TiB_2$/Cu 复合材料的力学性能与电导率

韩 非 [1,2,3]，姜伊辉 [1,2,3]，曹 飞 [1,2,3]，石 浩 [1,2,3]，蔡 磊 [1,2,3]，梁淑华 [1,2,3]

1. 西安理工大学 材料科学与工程学院，西安 710048；
2. 西安理工大学 教育部导电材料与复合技术工程研究中心，西安 710048；
3. 西安理工大学 陕西省电工材料与熔(浸)渗技术重点实验室，西安 710048

**摘 要：**针对传统方法制备的铜基复合材料力学性能与电导率之间的倒置关系，采用片状粉末冶金技术，以气雾化原位自生复合粉末为原料，制备了具有亚微米层厚度的 $TiB_2$/Cu−Cu 叠层复合材料。通过相邻异质片层之间的热失配强化、力学不兼容变形所产生的几何必需位错及其与统计储存位错之间的交互作用，所制备的 $TiB_2$/Cu−Cu 亚微米叠层复合材料获得了显著增强的力学性能。同时，多种模式裂纹之间的反应和协同扩展提高了 $TiB_2$/Cu−Cu 亚微米叠层复合材料的抗断裂能力。此外，具有低晶界密度和位错密度且无 $TiB_2$ 颗粒的纯 Cu 片层为载流子的快速传输提供了低电子散射通道，从而保证了高电导率。

**关键词：**亚微米叠层复合材料；热失配强化；不兼容变形；异质变形诱导强化；裂纹扩展

**(Edited by Wei-ping CHEN)**